

CrossMark
click for updatesCite this: *J. Mater. Chem. A*, 2014, 2, 15575

Hierarchical amorphous nanofibers for transparent inherently super-hydrophilic coatings†

William S. Y. Wong,^a Noushin Nasiri,^a Alexandra L. Rodriguez,^b David R. Nisbet^b and Antonio Tricoli^{*a}

Ultra-high specific surface area, hierarchical TiO₂ nanofibers were synthesized by electrospinning and directly self-assembled into highly porous films for application as transparent super-hydrophilic coatings. The evolution of the coating key structural properties such as fiber morphology and composition was mapped from the as-prepared sol-gel up to a calcination temperature of 500 °C. Main fiber restructuring processes such as formation of amorphous Ti–O bonds, crystallization, polymer decomposition and the organic removal were correlated to the resulting optical and wetting performance. Conditions for low-temperature synthesis of hierarchical coatings made of amorphous, mesoporous TiO₂ nanofibers with very high specific surface area were determined. The wetting properties of these amorphous and crystalline TiO₂ nanofiber films were investigated with respect to the achievement of inherently super-hydrophilic surfaces not requiring UV-activation. The surface stability of these amorphous TiO₂ nanofibers was assessed against current state-of-the-art crystalline super-hydrophilic TiO₂ preserving excellent anti-fogging performance upon an extended period of time (72 h) in darkness.

Received 27th June 2014
Accepted 6th August 2014

DOI: 10.1039/c4ta03278k

www.rsc.org/MaterialsA

Introduction

Since their first synthetic fabrication over a decade ago, super-hydrophilic surfaces have attracted substantial scientific interest¹ as they achieve a water sheeting effect within a very short timeframe (*ca.* 0.5 s).^{2–4} The resulting implications with respect to the condensation, evaporation and transport of (non- and atmospheric) water have led to their consideration for numerous commercial applications, including anti-fogging,^{5,6} self-cleaning,⁷ anti-fouling,⁸ bio-implants,⁹ micro-lenses,¹⁰ lab-on-a-chip,¹¹ microfluidics,^{6,12} fog-harvesting,¹³ and heat transfer enhancement.¹⁴

Several lab-scale methods have been successfully established for the synthesis of super-hydrophilic coatings including plasma, electrochemical treatment,⁶ reactive ion etching,⁵ micropatterning^{8,13} and flame spray pyrolysis.¹⁵ However, their wetting mechanism is still intensely debated. The complete spreading of a water droplet on a surface (perfect wetting) is expected on materials having high water affinity such as that generated by high surface concentrations of hydroxyl (–OH) groups.^{16,17} As a result, ideal super-hydrophilicity leads to a

contact angle (θ) nearing 0 and is achieved, according to Young's equation, for:

$$\gamma_s \geq \gamma_l + \gamma_{sl} \quad (1)$$

where γ_s is the solid surface free energy, γ_l is the liquid surface free energy (surface tension), γ_{sl} is the solid/liquid interfacial free energy. Given that this is the case for many materials (with the notable exception of organic polymers),¹⁸ super-hydrophilicity should be fairly common. However, spontaneous super-hydrophilic surfaces are rarely observed. This is usually attributed to the presence of a layer of volatile organics/gas molecules rapidly adsorbing onto the surfaces of these materials.^{19,20} To overcome these limitations, morphological modifications such as surface texturing have been utilized to enhance chemically-driven water spreading over that of perfectly flat surfaces.²¹

Titanium dioxide (TiO₂) is a widely utilized photocatalytic and ultraviolet (UV)-augmented material with high H₂O affinity that has been investigated for its photoactive,^{22,23} self-cleaning,^{23,24} optical²⁵ and chemical sensing²⁶ properties. Traditionally, the super-hydrophilicity of TiO₂ films has been found to correlate closely to UV exposure.^{1,27,28} For instance, UV-induced super-hydrophilicity has been investigated using thin sol-gel-made polycrystalline TiO₂ films annealed at 500 °C. These films required surface activation, becoming super-hydrophilic when exposed to UV irradiation and hydrophobic when kept in the dark.¹ Similar behaviors have been observed for amorphous

^aNanotechnology Research Laboratory, Research School of Engineering, Australian National University, Canberra 0200, Australia. E-mail: antonio.tricoli@anu.edu.au

^bLaboratory of Advanced Biomaterials, Research School of Engineering, Australian National University, Canberra 0200, Australia

† Electronic supplementary information (ESI) available: TGA, DTG. See DOI: 10.1039/c4ta03278k

TiO₂ films.^{27,28} This is a main limitation of TiO₂ that is known to lose super-hydrophilicity within a few minutes²⁰ to one day^{19,29,30} upon last exposure to UV-light.

Doping of sol-gel-made TiO₂^{3,29} and mesoporous surface enhancement³¹ have been used to promote UV-independent super-hydrophilicity. Highly rough TiO₂ films deposited by metal-organic vapor deposition were found to prevent the oxidation of Ti³⁺ during periods of darkness and were able to maintain super-hydrophilicity for extended periods (2–3 days) post UV-activation.³² Amongst other TiO₂ synthesis methods, electrospinning is a scalable, atmospheric process that offers several structural advantages. Electrospun coatings are continuously self-assembled during fiber synthesis, leading to a very porous multi-layer structure having considerably higher flexibility than PVD/CVD-made films^{32,33} and mechanical stability than aerosol-deposited nanoparticle layers.^{15,34} Electrospinning of polyvinyl pyrrolidone–titanium(IV) isopropoxide (PVP–TTIP) sol-gel mixtures has led to some of the thinnest TiO₂ fibers so far reported.^{35,36} However, the optimization of electrospun TiO₂ nanofiber composition and morphology for fabrication of UV-independent, super-hydrophilic coatings has not yet been reported.

Here, the synthesis of amorphous TiO₂ nanofibers for the fabrication of transparent and inherently super-hydrophilic coatings has been investigated. The evolution of the key fiber structural properties was mapped as a function of calcination temperature in terms of morphology, bulk and surface compositions leading to a well-characterized set of amorphous and crystalline TiO₂ nanofiber coatings. Structural-functional correlations of these materials have been established with respect to their wetting and optical properties. A novel hierarchical amorphous TiO₂ nanofiber morphology with excellent anti-fogging performance was identified and compared to state-of-the-art anatase crystalline coatings.

Experimental

Materials and fabrication

Nanofibers were obtained by electrospinning of an ethanol-based sol-gel (0.06 g mL⁻¹ PVP and 0.0936 g mL⁻¹ Ti(OiPr)₄), with acetic acid as a hydrolysis promoter.³⁵ A PVP solution was first prepared by dissolving 0.6 g of PVP (Sigma Aldrich, *M_w* = 1 300 000) in 5 mL of ethanol (Sigma Aldrich, 200 proof). A sol-gel solution was then prepared using 2 mL of ethanol, 2 mL of acetic acid (glacial, Chem-Supply) and 1 mL of Ti(OiPr)₄ (Sigma Aldrich). Solutions were stirred for 10 minutes before introducing the sol-gel mixture into the PVP solution. A clear yellowish solution was obtained, which was electrospun after 1 hour of mixing. An applied voltage of 25 kV was used with a working distance and flow rate of 20 cm and 0.8 mL h⁻¹, respectively, providing homogenous coverage of nanofibers on the glass substrates. Surface coverage was confirmed by optical microscopy. A deposition time of 1 minute was used to obtain clear, transparent coatings. Once collected on glass slides, the coatings were stored at room temperature for 5–6 hours to allow for the completion of hydrolysis. Samples were then calcined for 1 hour (3 °C min⁻¹) between 100 °C and 500 °C (*T_s*).

Characterization

Calcined coatings were then kept in the dark at room temperature for 3 days before proceeding to the wetting studies. The dynamic water contact angle (CA) was measured by placing a drop of deionized water (5–6 μL) on the sample surface using a KSV CAM200 contact angle goniometer (Finland) with a heliopan ES43 camera (Japan). The CA was computed by a commercially available (CAM2008) program. Samples were analyzed using a Zeiss UltraPlus analytical scanning electron microscope (FESEM) at 3 kV and a Hitachi H7100FA 125 kV transmission electron microscope (TEM). Prior to examination, SEM specimens were platinum sputter-coated for 2 min at 20 mA. Average fiber diameters (*d_{EM}*) were determined by counting with ImageJ 20 fibers in each SEM image. TEM specimens were suspended and dispersed in ethanol (Sigma Aldrich, 200 proof) before they were deposited on 200-mesh nickel-copper grids (Formvar) and dried at room temperature. UV-vis analysis was conducted using a microplate reader (Tecan 200 PRO, Switzerland) from 300–800 nm with 10 scans per cycle. The crystal phases, size (*d_{XRD}*) and surface compositions were analyzed by X-ray diffraction (XRD, D2 Phaser, Bruker, U.S.A) and Fourier transform infrared spectroscopy (FTIR-ATR, Bruker-Alpha, U.S.A). Amorphous samples in XRD (< 400 °C) were normalized using the first crystalline anatase 101 peak achieved at 400 °C. The Brunauer–Emmett–Teller specific surface area (BET, SSA), pore volume and distribution of the as-prepared coatings were measured by N₂ adsorption using a porosity analyzer (Micromeritics, TriStar II, U.S.A). All samples were degassed at 300 °C for 5 hours prior to analysis. Evaluation of the antifogging performance was conducted on selected calcined coatings (300 °C, 350 °C, 500 °C) by exposure to a vapor stream 40 cm above boiling water for 5–10 s, as previously reported.¹⁵ Thermogravimetric (TGA) and differential thermogravimetry (DTG) analysis were conducted from 100–800 °C (3 °C min⁻¹ ramp) and isothermally at 350 °C for 1 h under atmospheric conditions (Perkin Elmer, STA 8000, U.S.A).

Results and discussion

Synthesis and characterization of hierarchical nanofibers

The as-prepared nanofibers had a flexible structure with notable formation of hoop and spiral shapes (Fig. 1a) upon evaporation of the solvent utilized for TEM preparation. Their appearance was flaky, revealing a porous morphology and a very rough surface. Upon low temperature (*T_s* = 250–350 °C) calcination, the fibers' diameters shrunk rapidly (Fig. 1b and c) leading to increased rigidity and relatively smooth surface morphologies. Increasing the calcination temperature to 500 °C had minimal impact on the fiber size but increased surface roughness, resulting in a granular appearance with a grain size of *ca.* 20 nm (Fig. 1d, inset). This is in line with previous reports on high-temperature calcined TiO₂ fibers,²⁵ attributing this morphology to crystal nucleation.

The SEM analysis (Fig. 2) of the coatings supported these observations with the average fiber count diameter decreasing

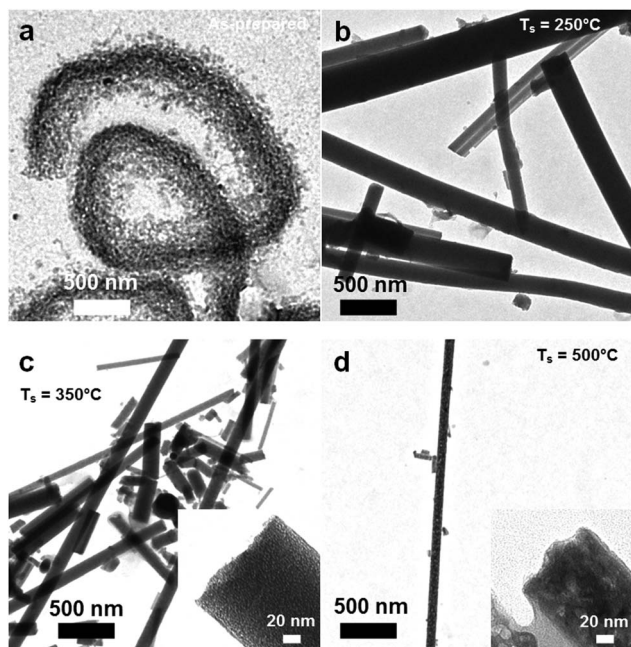


Fig. 1 TEM images of (a) as-prepared and calcined at (b) 250 °C, (c) 350 °C and (d) 500 °C TiO₂ nanofibers.

from 412 nm ± 104 nm of the as-prepared (Fig. 2a) to 80.8 nm ± 44.5 nm of the 500 °C calcined samples (Fig. 2f). The largest reduction in fiber diameters from 210 to 128 nm was observed with increasing temperature from 300 to 350 °C. Detailed analysis from 350 to 500 °C revealed that roughening and restructuring of the fiber surface occurs for $T_s \geq 400$ °C. This was in-line with the granular morphology observed by TEM (Fig. 1d, inset) and is attributed to the nucleation of TiO₂ crystals on the nanofiber surfaces (Fig. 2d).

Although the visible TEM and SEM fiber diameter decreased monotonously with increasing calcination temperature, the available surface for water adsorption was maximal below 500 °C. Fig. 4a shows the specific surface area (SSA) of the fibers (Fig. 4a, triangles) as a function of the calcination temperature.

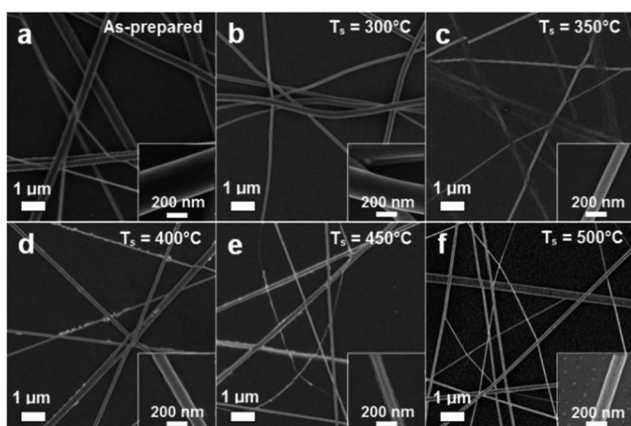


Fig. 2 SEM images of (a) as-prepared and calcined fibers at (b) 300 °C, (c) 350 °C, (d) 400 °C, (e) 450 °C and (f) 500 °C.

The SSA increased drastically from *ca.* 65 to 106 m² g⁻¹ with increasing T_s from 300 to 350 °C. This is only partially justified by the fiber diameter reduction observed by SEM and TEM (Fig. 2b and c). This surface restructuring is attributed to the desorption of (PVP) polymer residuals.

The XRD spectra of the calcined samples (Fig. 3) provided further understanding of the observed surface restructuring (Fig. 1 and 2). Up to a calcination temperature of 350 °C, the TiO₂ nanofibers were amorphous with no visible diffraction peaks (Fig. 3). At T_s of 400 °C, anatase crystals with an average size of 8.8 nm were nucleated. Further increasing T_s (450 °C) increased the crystal size to 12.0 nm preserving the pure anatase structure. At 500 °C, the formation of a small amount (8.2 wt%) of rutile was observed and the anatase d_{XRD} reached 17.4 nm. This is in line with the TEM morphology observed at 500 °C and suggests that the multi-granular texture of the fibers is caused by the formation of large anatase crystals.

Increasing the calcination temperature step-wise to 500 °C resulted in a 50% SSA reduction. This was characterized by an initial SSA drop to 42 ± 5 m² g⁻¹ at 450 °C and thereafter its leveling-off up to 500 °C. Considering that the fiber diameter of the 350 °C calcined samples was slightly larger than that of the 500 °C ones, the higher SSA of amorphous TiO₂ nanofibers indicates the formation of a mesoporous surface morphology. This is further supported by the large pore volume and small (4.7 nm) average pore size measured upon partial removal of the organic scaffold at 350 °C (Table 1).

At a higher magnification (Fig. 1c, inset) the smooth-appearing fibers calcined at 350 °C had a more discrete structure, suggesting the presence of nano-scale pores. The high SSA achieved here by these amorphous nanostructures ($T_s = 350$ °C) is comparable to the highest reported for TiO₂ nanofibers^{26,37,38} and is, to the best of our knowledge, also the highest ever achieved with the PVP-TTIP system. The hierarchical morphology of these amorphous fiber coatings combines the

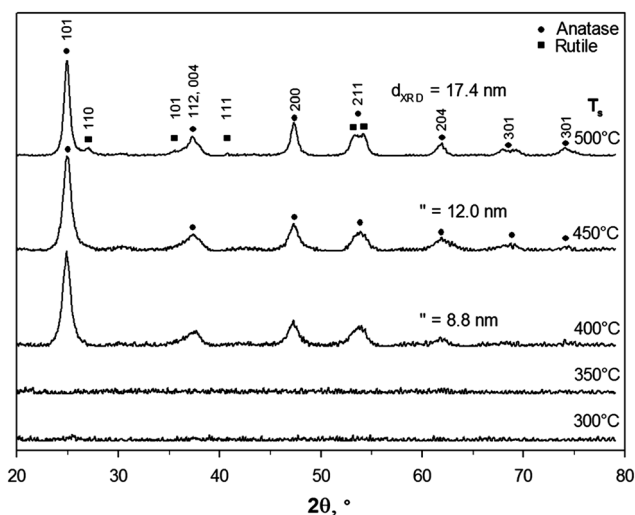


Fig. 3 XRD spectra of the calcined fibers and corresponding anatase and rutile phase peaks. The average crystal size was 8.8, 12.0 and 17.4 nm for the 400, 450 and 500 °C samples.

Table 1 Properties and performance of the TiO₂ fibers, and comparison with selected literature data^a

Morphology	d_{EM} nm	SSA m ² g ⁻¹	PV cm ³ g ⁻¹	CA _i °	CA _d °	Ref.
Amorphous TiO ₂ fibers $T_s = 350$ °C	128	105.8	0.100	8.5	9.2	This work
92 wt% Anatase fibers $T_s = 500$ °C	81	44.8	0.076	0.0	7.0	This work
ES anatase fibers	150	60	—	2.0	—	23
ED amorphous NPs	—	—	—	12	39	27
FSP NPs	—	—	—	5–8	10	15

^a d_{EM} – fiber diameter determined by electron microscopy. PV – pore volume of fibers. CA_i – initial contact angle upon synthesis. CA_d – contact angle after incubation in darkness for >12 hours. ED – Electrodeposited. FSP – Flame spray pyrolysis. ES – Electrospun. NPs – Nanoparticles.

macro-scale porosity of the fiber layers (Fig. 2c) with the nano-scale roughness of their mesoporous surface (Fig. 4a and b) offering an optimal structure for the rapid penetration and spreading of water.

Optical and wetting performance

The optical performance of the nanofiber coatings was investigated as a function of the calcination temperature. Fig. 5 shows the transmittance at an incoming light wavelength of 400 nm (circles) and 600 nm (triangles) from the as-prepared to the

500 °C calcined samples. The as-prepared coatings' transmittance was *ca.* 77.5% for both wavelengths. This was attributed to the presence of PVP and large fiber diameters (*ca.* 440 nm), leading to strong light scattering and absorption. Calcining the samples to 250 °C increased transmittance by *ca.* 10%, in line with the suggested partial decomposition and desorption of the PVP matrix.

Increasing T_s to 350 °C gradually increased the transmittance up to *ca.* 92.5% and thus *ca.* 2.5% below that of the bare glass slides. Further increments in T_s (up to 500 °C) did not enhance light transmittance. This is in line with the stabilization of the fiber diameter observed by SEM and TEM (Fig. 1 and 2) and the relatively small amount of organic residuals detected by FTIR at 350 °C (Fig. 8). Transmittance values between 85%²⁴ to 90%²³ are considered sufficient for most optical applications. The optical performance obtained here is comparable to state-of-the-art coatings,^{23,24} showcasing the suitability of these amorphous nanofibers for applications in micro-lenses, solar cells and photo-detectors.

The long-term coating wetting properties were quantified as a function of the calcination temperature by measurement of the dynamic contact angle with a water droplet upon keeping the samples in the dark for 72 h (CA_d). Fig. 6 compares the

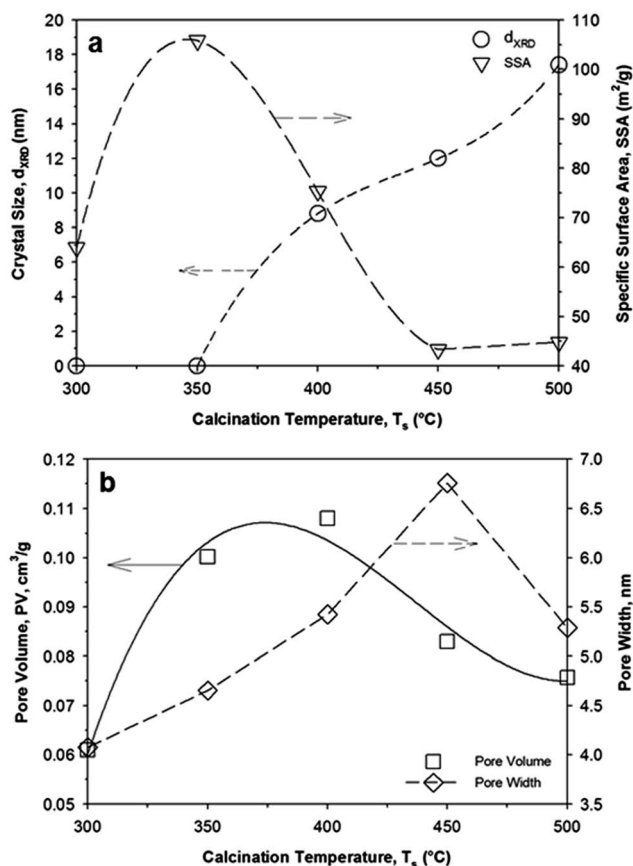


Fig. 4 (a) Average crystal size (d_{XRD} , circles) and specific surface area (SSA, triangles) as a function of the calcination temperature (T_s). (b) Pore volume (PV, squares) and pore width (PW, diamonds) as a function of calcination temperature (T_s).

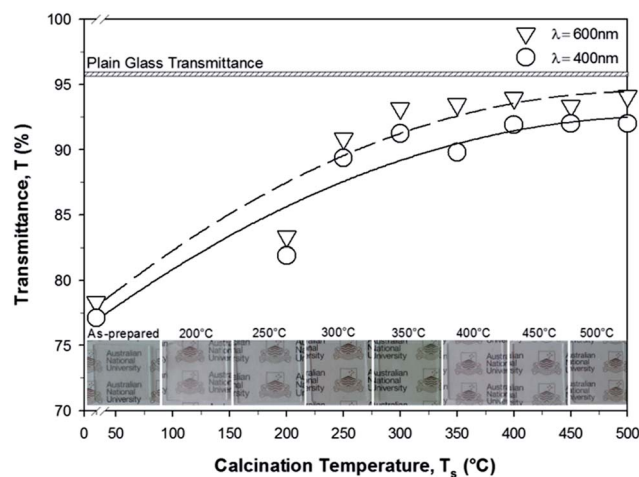


Fig. 5 Light transmittance through the coatings at a wavelength of 400 nm (circles) and 600 nm (triangles) as a function of the calcination temperature.

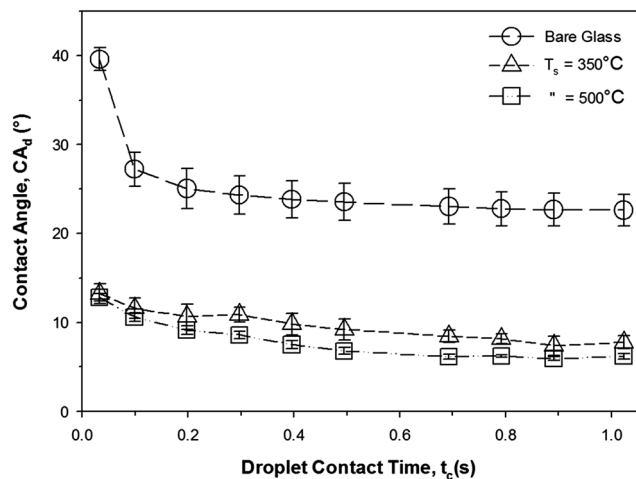


Fig. 6 Dynamic water contact angle of bare (circles) and TiO₂ nanofibers coated glasses calcined at (triangles) 350 °C and (squares) 500 °C after 72 hours in the darkness.

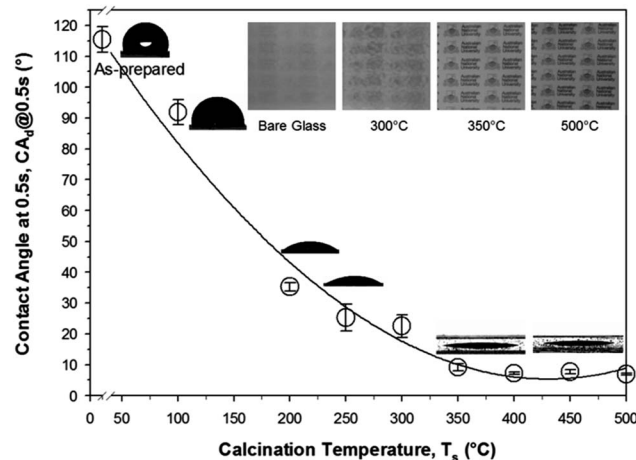


Fig. 7 Dynamic water contact angle and (insets) optical images of water droplets as a function of the calcination temperature. Optical images (top right insets) of bare and coated glass in a water vapor stream.

dynamic water contact angle for the 350 °C (triangles) and 500 °C (square) calcined coatings with bare glass (circles).

Upon a contact time of 0.5 s, the CA_d of the bare glass converged toward *ca.* 25°. In contrast, the glass with the 350 °C and 500 °C coatings reached a CA_d of *ca.* 8.1 ± 1° (t_c = 0.5 s). Although the latter had a slightly lower CA_d (Table 1), these effects were minimal, and the actual performance was almost indistinguishable with both coatings satisfying super-hydrophilic requirements. This is attributed to the larger SSA and pore volume of the amorphous fibers (Table 1) compensating for the higher H₂O affinity of the anatase surface. It is worth noticing that the initial contact angle at 0.5 s (CA_i) of the 500 °C samples (Table 1) was 0° indicating a partial deactivation of the anatase surface upon 72 h in darkness. In contrast, for the amorphous fibers the initial (8.5°) and post-light deprivation

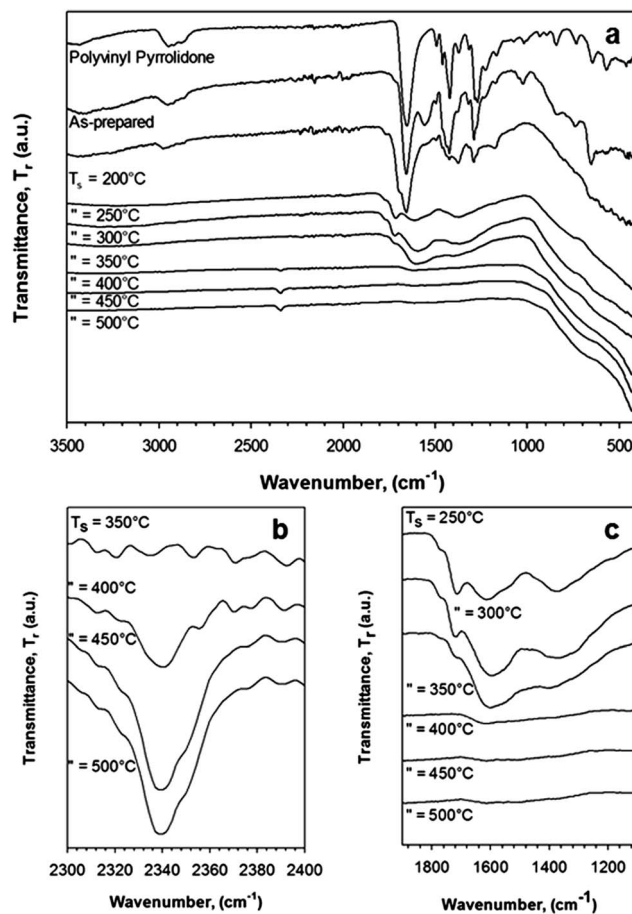


Fig. 8 FTIR spectra (a) of electrospun TiO₂ nanofibers as a function of the calcination temperature (T_s). Magnifications of the FTIR spectra from (b) from 2300 cm⁻¹ to 2400 cm⁻¹ depicting atmospheric CO₂ adsorption, and (c) from 1100 cm⁻¹ to 1900 cm⁻¹ depicting the loss of organics between 250–400 °C.

(9.2°) contact angles (Table 1) were nearly identical suggesting inherent super-hydrophilicity.

Fig. 7 shows the initial dynamic water contact angle at 0.5 s as a function of the calcination temperature. The as-prepared coatings (Fig. 7) were hydrophobic with a CA of 115°. The CA_d decreased sharply with increasing calcination temperature with an asymptotic behavior. The largest CA drop occurred from 100 to 250 °C (CA_{d,250 °C} = 25°). Further increasing T_s to 350 °C led to a CA_d of below 10° and thus to the attainment of super-hydrophilicity (CA_{d,350 °C} = 9.2°). Small reductions (≈ 1°) in CA were obtained for T_s ≥ 400 °C. To assess the durability of the films, subsequent multi-drop tests were conducted on the 350 °C and 500 °C calcined films. No variation of the water contact angle and macroscopic film structure was observed up to 6 hours wetting-drying cycles.

The coating anti-fogging performance was assessed by placing the bare and coated glass slides in a water vapor stream. Uncoated glass fogged within a few seconds due to the condensation of water droplets (Fig. 7, insets). The coating calcined at 300 °C demonstrated reduced fogging and improved transmittance. However, the background visibility was still

severely hindered by partial fogging. The coatings calcined at $T_s \geq 350$ °C demonstrated excellent anti-fogging performance with a clear and transparent appearance during the entire period of vapor exposure. This indicates that both a mesoporous surface and removal of most organics are required to obtain super-hydrophilicity. These results show, for the first time, that low-temperature synthesized amorphous TiO_2 , not requiring UV-activation, can achieve comparable wetting performance as crystalline anatase assembled at high-temperatures.

Nanofiber surface analysis

To explain the strong variation in wetting and anti-fogging performance observed from 300 to 350 °C, the fiber surface composition was investigated by FTIR. The onset of PVP scaffold decomposition was found to take place between 250–350 °C, in line with previous reports^{39,40} where diminishing organic peaks⁴¹ such as C=O stretch at 1650 cm^{-1} , CH_2 scissor at 1419 cm^{-1} , CH_2 twist, wag and C–N stretch at $1200\text{--}1300\text{ cm}^{-1}$ occurred. The Ti–O bonds were found to become predominant at a calcination temperature of 250 °C as indicated by strong inorganic Ti–O peaks⁴² between $450\text{--}550\text{ cm}^{-1}$. This explains the strong drop in contact angle ($\Delta\text{CA} = 90^\circ$) observed for calcination temperatures above 200 °C (Fig. 7).

Further increasing the calcination temperature led to a reduction of organic related peaks that completely disappeared only at 400 °C. These findings further indicate that the fiber diameter shrinkage dynamics is controlled by the decomposition and desorption of the polymer precursor (Fig. 1 and 2). The remaining organic peaks ($\sim 1650\text{ cm}^{-1}$) at 350 °C were mostly attributed to distorted C=O, and appeared to have a minimal impact on the surface water affinity (Fig. 7). A peak at 2340 cm^{-1} was also found for $T_s \geq 400$ °C, suggesting the presence of physisorbed carbon dioxide (CO_2). This is in line with previous reports indicating considerable adsorption of atmospheric CO_2 on crystalline TiO_2 . It is worth noting that, even after an extended incubation period of 8 days, the amorphous TiO_2 ($T_s = 350$ °C) did not develop this CO_2 peak (not shown). This is in line with the TGA analysis of the fiber mats (Fig. S1†) showing that most of the organics are desorbed between 300 and 400 °C. Furthermore, analysis of the organics desorption dynamics at isothermal conditions (Fig. S2†) suggests that the critical transitional temperature for organics removal and achievement of super-hydrophilicity is close to 350 °C.

Conclusions

An optimal TiO_2 nanofiber morphology was determined for fabrication of flexible, non-UV augmented super-hydrophilic coatings having superior transparency and anti-fogging performance. For the first time, it is shown that very-high SSA ($>100\text{ m}^2\text{ g}^{-1}$), hierarchical, amorphous TiO_2 nanofibers, not requiring UV activation, have comparable inherent wetting performance to crystalline anatase. These amorphous fiber coatings were synthesized by rapid (1 min) electrospinning leading to enhanced and prolonged (72 h in the darkness) super-hydrophilicity. It was found that amorphous Ti–O bonds

become predominant at 250 °C leading to a considerable reduction ($\Delta\text{CA} = 90^\circ$) of the water contact angle. Calcination at 350 °C was required to remove most residual organics and obtain quasi-perfect wetting (CA_d at 0.5 s $<10^\circ$). These low-temperature synthesized amorphous nanofibers have potential for development of super-hydrophilic coatings with numerous applications such as anti-fog glass, microfluidic devices and water filtration membranes.

Acknowledgements

We thank Prof. Vincent Craig, Prof. Tim Senden (RSPE, ANU), Dr. Adrian Lowe (RSE, ANU) and Prof. Takuya Tsuzuki (RSE, ANU) for their valuable advice and the use of their laboratories. WSYW acknowledges the PhD research fellowship from the Australian National University. ALR was supported by an Australian Postgraduate Award; DRN was supported by an Australian Research Council Australian Postdoctoral Fellowship, and subsequently by a NHMRC Career Development Fellowship. AT was supported by a Future Engineering Research Leadership (FERL) fellowship. This work was partially supported by the ANU-Discovery Translation Fund grant (DTF078).

Notes and references

- 1 R. Wang, K. Hashimoto, A. Fujishima, M. Chikuni, E. Kojima, A. Kitamura, M. Shimohigoshi and T. Watanabe, *Nature*, 1997, **388**, 431–432.
- 2 D. Glöß, P. Frach, O. Zywitzki, T. Modes, S. Klinkenberg and C. Gottfried, *Surf. Coat. Technol.*, 2005, **200**, 967–971.
- 3 M. Machida, K. Norimoto, T. Watanabe, K. Hashimoto and A. Fujishima, *J. Mater. Sci.*, 1999, **34**, 2569–2574.
- 4 F. Ç. Cebeci, Z. Wu, L. Zhai, R. E. Cohen and M. F. Rubner, *Langmuir*, 2006, **22**, 2856–2862.
- 5 D. Tahk, T.-i. Kim, H. Yoon, M. Choi, K. Shin and K. Y. Suh, *Langmuir*, 2010, **26**, 2240–2243.
- 6 P. Patel, C. K. Choi and D. D. Meng, *JALA*, 2010, **15**, 114–119.
- 7 R. Blossey, *Nat. Mater.*, 2003, **2**, 301–306.
- 8 M. L. Carman, T. G. Estes, A. W. Feinberg, J. F. Schumacher, W. Wilkerson, L. H. Wilson, M. E. Callow, J. A. Callow and A. B. Brennan, *Biofouling*, 2006, **22**, 11–21.
- 9 H. Thissen, T. Gengenbach, R. du Toit, D. F. Sweeney, P. Kingstott, H. J. Griesser and L. Meagher, *Biomaterials*, 2010, **31**, 5510–5519.
- 10 B. H. W. Hendriks, S. Kuiper, M. A. J. As, C. A. Renders and T. W. Tukker, *Opt. Rev.*, 2005, **12**, 255–259.
- 11 S. Shahi, *Nat. Photonics*, 2010, **4**, 350.
- 12 E. Ueda and P. A. Levkin, *Adv. Mater.*, 2013, **25**, 1234–1247.
- 13 R. P. Garrod, L. G. Harris, W. C. E. Schofield, J. McGettrick, L. J. Ward, D. O. H. Teare and J. P. S. Badyal, *Langmuir*, 2006, **23**, 689–693.
- 14 C. Li, Z. Wang, P. I. Wang, Y. Peles, N. Koratkar and G. P. Peterson, *Small*, 2008, **4**, 1084–1088.
- 15 A. Tricoli, M. Righettoni and S. E. Pratsinis, *Langmuir*, 2009, **25**, 12578–12584.
- 16 M. Harju, E. Levänen and T. Mäntylä, *Appl. Surf. Sci.*, 2006, **252**, 8514–8520.

- 17 M. M. Gentleman and J. A. Ruud, *Langmuir*, 2009, **26**, 1408–1411.
- 18 S. Wu, *Polymer Interface and Adhesion*, Taylor & Francis, 1982.
- 19 A. Mills and M. Crow, *Int. J. Photoenergy*, 2008, **2008**, 1–6.
- 20 A. Kanta, R. Sedev and J. Ralston, *Langmuir*, 2005, **21**, 2400–2407.
- 21 J. Drelich and E. Chibowski, *Langmuir*, 2010, **26**, 18621–18623.
- 22 Q. Li, D. Sun and H. Kim, *Mater. Res. Bull.*, 2011, **46**, 2094–2099.
- 23 V. A. Ganesh, A. S. Nair, H. K. Raut, T. M. Walsh and S. Ramakrishna, *RSC Adv.*, 2012, **2**, 2067.
- 24 F. Li, Q. Li and H. Kim, *Appl. Surf. Sci.*, 2013, **276**, 390–396.
- 25 A. Kumar, R. Jose, K. Fujihara, J. Wang and S. Ramakrishna, *Chem. Mater.*, 2007, **19**, 6536–6542.
- 26 I.-D. Kim, A. Rothschild, B. H. Lee, D. Y. Kim, S. M. Jo and H. L. Tuller, *Nano Lett.*, 2006, **6**, 2009–2013.
- 27 S. Karuppuchamy and J. M. Jeong, *Mater. Chem. Phys.*, 2005, **93**, 251–254.
- 28 Y. Gao, Y. Masuda and K. Koumoto, *Langmuir*, 2004, **20**, 3188–3194.
- 29 K. Guan, *Surf. Coat. Technol.*, 2005, **191**, 155–160.
- 30 A. Eshaghi and A. Eshaghi, *Bull. Mater. Sci.*, 2012, **35**, 137–142.
- 31 A. S. Zuruzi, Y. H. Yeo, A. J. Monkowski, C. S. Ding and N. C. MacDonald, *Nanotechnology*, 2013, **24**, 245304.
- 32 H. Y. Lee, Y. H. Park and K. H. Ko, *Langmuir*, 2000, **16**, 7289–7293.
- 33 J.-M. Wu, H. C. Shih and W.-T. Wu, *Chem. Phys. Lett.*, 2005, **413**, 490–494.
- 34 A. Tricoli, M. Graf, F. Mayer, S. Kuühne, A. Hierlemann and S. E. Pratsinis, *Adv. Mater.*, 2008, **20**, 3005–3010.
- 35 D. Li and Y. Xia, *Nano Lett.*, 2003, **3**, 555–560.
- 36 S. H. Hwang, C. Kim, H. Song, S. Son and J. Jang, *ACS Appl. Mater. Interfaces*, 2012, **4**, 5287–5292.
- 37 W. Zhang, R. Zhu, L. Ke, X. Liu, B. Liu and S. Ramakrishna, *Small*, 2010, **6**, 2176–2182.
- 38 P. S. Kumar, S. A. S. Nizar, J. Sundaramurthy, P. Ragupathy, V. Thavasi, S. G. Mhaisalkar and S. Ramakrishna, *J. Mater. Chem.*, 2011, **21**, 9784.
- 39 D. Dollimore and G. R. Heal, *Carbon*, 1967, **5**, 65–72.
- 40 M. I. Loria-Bastarrachea, W. Herrera-Kao, J. V. Cauich-Rodríguez, J. M. Cervantes-Uc, H. Vázquez-Torres and A. Ávila-Ortega, *J. Therm. Anal. Calorim.*, 2010, **104**, 737–742.
- 41 Y. Borodko, S. E. Habas, M. Koebel, P. Yang, H. Frei and G. A. Somorjai, *J. Phys. Chem. B*, 2006, **110**, 23052–23059.
- 42 N. B. Colthup, L. H. Daly and S. E. Wiberley, *Introduction to infrared and Raman spectroscopy*, Academic Press, 1990.